Tiling the plane with noncongruent toric focal conic domains

Christophe Blanc* and Maurice Kleman
Laboratoire de Minéralogie-Cristallographie de Paris, CNRS UMR No. 7590, T16 case 115, Université Pierre et Marie Curie, 4 Place Jussieu, F-75252 Paris Cedex 05, France
(Received 27 May 2000)

This paper deals with regular arrays of macroscopic defects (focal conic domains) observed when a slab of lamellar phase is sandwiched between two substrates imposing different *orientational* anchorings. We report, in particular, detailed observations of the texture of a lyotropic lamellar phase in contact with a glass substrate and a lyotropic sponge phase. We consider several models for the defects depending on the material and the substrate parameters. Their energy has a common form, and the main features of the textures are explained in the framework of a simple model where disks of different sizes tile a plane in order to minimize a particular interface energy.

PACS number(s): 61.30.Jf, 68.10.Cr

I. INTRODUCTION

Lamellar liquid crystal phases, which consist of a periodic stack of parallel surfaces, occur in different materials such as thermotropic liquid crystals or surfactant-solvent mixtures. On a large scale, they share some common behaviors which are related to their one-dimensional crystal nature, and not to their specific microscopic structure. This is particularly revealing when macroscopic defects are involved. For example, focal conics domains (FCD's), which are made of parallel layers folded along Dupin cyclides [1,2], are the classic macroscopic defects of the thermotropic smectic-*A* (Sm*A*) materials, but are also observed in the lamellar L_α lyotropic phases [3–5].

FCD's are often unstable defects, frozen in a smectic sample during its preparation, and they disappear when the sample is annealed. In confined lamellar phases, however, the macroscopic defects are necessarily present in order to satisfy different anchorings at the interfaces. One of the most spectacular illustration of this phenomenon is the formation of regular lattices of TFCD's (toric focal conics domains) in a thin slab of Sm*A* material sandwiched between its isotropic melt and the air (Fig. 1).

These lattices were first reported at the beginning of the last century by Friedel [1], but their appearance was accurately studied only much later [6–8]. The antagonistic boundary conditions—parallel anchoring of the layers at the Sm*A*-air interface vs perpendicular orientation at the isotropic-Sm*A* interface (see Fig. 2)—are the driving force of a texture instability which appears above a critical thickness. A transition is indeed observed between a homeotropic geometry, where the orientation of the layers is imposed by the air, and the nucleation of defects when the thickness of the smectic sample increases. The defects are TFCD's, which display a singular line along their axis of revolution and a quasivirtual singular circle, sitting at the Sm*A*-isotropic interface (see Fig. 2).

Apart from the study of the nucleation of isolated defects, several factors have limited a further study of the equilibrium textures. Due to the strong first-order character of the transition, hysteretic phenomena are indeed present, and the textures are not perfectly reproducible above the critical thickness in the thermotropic liquid crystals which have been used [6]. Moreover, from a theoretical viewpoint, the models built so far deal only with isolated defects, whereas the patterns formed by these defects have not been studied. However, it should be noted that several theoretical models in the past considered the tiling of a plane with focal conic domains. The most popular model is the Apollonius tiling (see Fig. 3), where small TFCD's (represented here by their singular circle) iteratively fill the interstices between larger ones. This model is clearly not fit to explain the regular lattices that have been observed.

Similar arrays of defects (see Fig. 4) were recently reported [9] in a lyotropic lamellar system sandwiched between a glass substrate and a sponge phase (the isotropic sponge phase is also a phase of membranes, but is usually described by a single disordered and multiply connected membrane which divides the solvent into two equivalent subvolumes; see details in Refs. [10–14]). The appearance of defects in a slab of lamellar phase is also due to the compe-

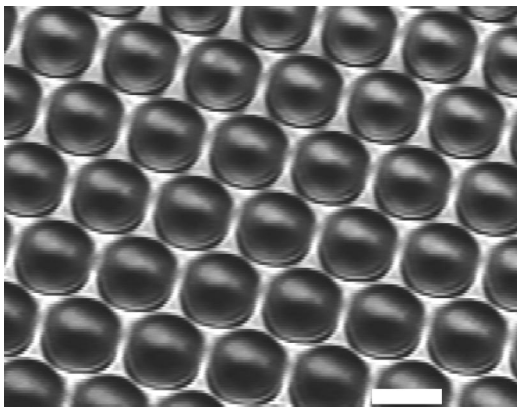

FIG. 1. A thin slab of Sm*A* phase between air and its isotropic melt is unstable toward the formation of macroscopic defects. This micrograph was obtained with the thermotropic liquid crystal 4,4′ diethyl azoxydibenzoate, which undergoes a smectic-to-isotropic transition at 120 °C. Bar is approximately equal to 20 μm.

*Electronic address: blanc@lmcp.jussieu.fr

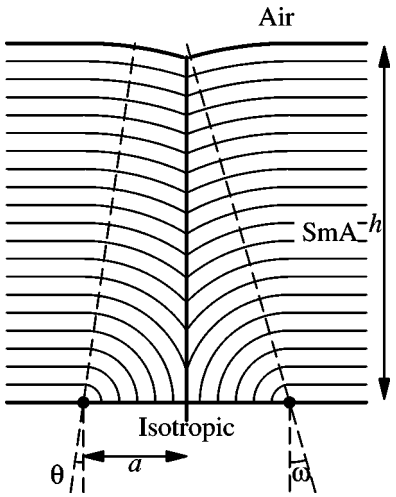

FIG. 2. Geometric model of the macroscopic defects of Fig. 1 proposed by J.-B. Fournier, I. Dozov, and G. Durand, Phys. Rev. A **41**, 2252 (1990). The layers are part of a toric focal conics domain (TFCD) and the singular lines consist of a straight line (along the axis of revolution) and a circle sitting on the isotropic Sm*A* interface. Note that a small depression is expected at the air-Sm*A* interface.

tition between different anchorings at the glass/L_α interface and at the L_α/L_3 interface. The layers are parallel to the glass substrates whereas they are strongly tilted at an angle θ_0 near the L_3 phase. Contrary to the thermotropic case, hexagonal lattices of defects observed just above a critical thickness are reproducible. In a recent paper [15] we proposed a simple model which explains the observed quantitative evolution of the defect lattice parameter with the thickness of the lamellar slab. The aim of the present paper is, first, to extend this model to thick slabs and to different experimental situations and, second, to discuss the observed textures on a scale larger than one defect. In particular, we show that our model predicts the disappearance of a hexagonal lattice above a second critical thickness, and the appearance of other patterns.

The paper is structured as follows. In Sec. II, we present

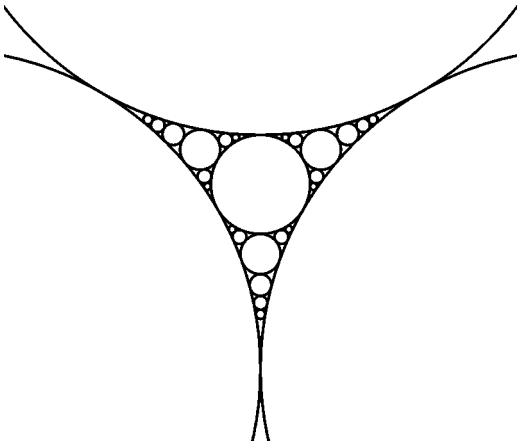

FIG. 3. The Apollonius tiling consists of packed circles that fill the plane iteratively. Such a model can be used to propose a texture made of toric focal conics domains which ensures a planar anchoring everywhere at the isotropic-Sm*A* interface.

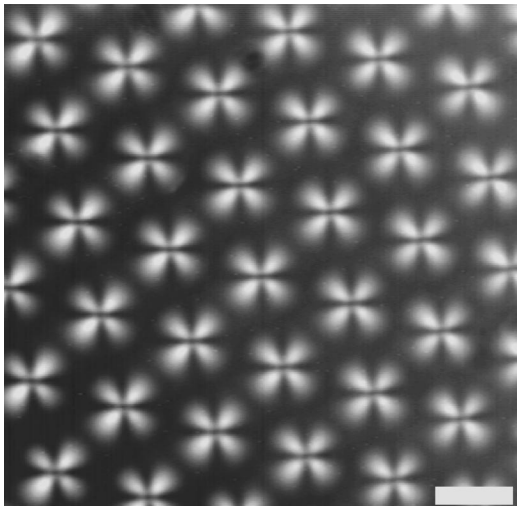

FIG. 4. A thin slab of lamellar phase sandwiched between glass and sponge phases displays an hexagonal array of defects (thickness is approximately equal to 100 μm, and bar to 20 μm).

experimental observations of lamellar textures confined between the sponge phase and the glass substrate, and show that the simple hexagonal lattice is an equilibrium pattern for small thicknesses, whereas other textures appear at larger thicknesses. In Sec. III, we consider the most common experimental situations for a confined smectic slab, and show that the free energy of a single defect has the same form. We also show that the main experimental features of the lattice are explained by the minimization of a particular interface energy. In Sec. IV we then discuss the dynamics of the defects and textures.

II. OPTICAL MICROSCOPY OBSERVATIONS

A. Experimental system

The system which has been studied is a mixture of cetylpyridinium chloride (CPCl), hexanol and solvent (water with 1 wt.% of NaCl). For the brine weight fraction $\phi_w = 0.7$, the domain of coexistence between the L_3 and L_α phases is found for a weight ratio of hexanol over CPCl h/c between 1.05 and 1.11.

A thin slab of lamellar phase confined between the sponge phase and the lamellar phase is submitted to two different anchorings [15]. The glass gives a homeotropic orientation, whereas the layers are strongly tilted at the L_α/L_3 interface with an angle θ_0 close to 70° for this dilution [9]. The system responds to this frustration by the formation of defects.

The experimental formation of the L_α slab can be obtained in two different ways. First [15], we used the fact that the L_3 phase changes to the lamellar phase when increasing the temperature. A sample of the L_3 phase at room temperature ($h/c \approx 1.115-1.120$) is introduced in a glass capillary (Vitrodynamics, thickness 200, 300, or 400 μm) which is sealed by the flame. The sample is heated in the domain of coexistence ($T \approx 40\,^\circ$C). When the rate of temperature increase is small enough (below $0.1-0.2\,^\circ\mathrm{C\,min^{-1}}$) the lamellar phase grows slowly from the glass substrate but does not appear in the bulk in the form of nuclei. Above a critical thickness $h_{c,1}$, a hexagonal lattice of defect appears (see Fig. 4). Due to the slow growth of the lamellar phase, organized

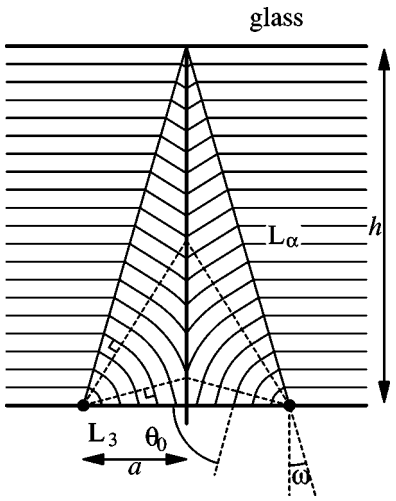

FIG. 5. The layers of the lamellar phase cannot satisfy both the homeotropic anchoring on the glass substrate and the tilt angle at the lamellar-sponge interface. A small-angle curvature wall is experimentally observed. The curvature wall has an exact cone shape, and the two strong boundary conditions are satisfied everywhere inside the defects.

domains are observed on a large scale (typical size $\geqslant 1$ mm; see further details in Ref. [15]).

In the second method, either we prepare the sample in a domain of coexistence at room temperature (h/c between 1.05 and 1.11), or we quickly bring an L_3 sample ($h/c \approx 1.11-1.12$) into the domain of coexistence. The two phases, in both cases, are initially mixed in the bulk, but they separate slowly in a few hours. The L_α phase has a lower density, and settles on the upper glass substrate. Note that we have also used homemade cells in order to obtain thicknesses up to a few millimeters. These cells consist in pierced slides of Plexiglass in which we confine the sample by covering it with a cover glass. This latter is glued in order to avoid the evaporation of the sample. The samples prepared in these different ways are observed under an optical polarizing microscope Leitz (DMRXP) equipped with a hot stage (Mettler 82HT), a movie camera, and a movie recorder.

B. Observations

1. Defects of the regular lattices

We previously reported experimental observations of the appearance of hexagonal lattices (HL's) in thin slabs of lamellar phase (thickness $h \leqslant 200$ μm), and the existence of a critical thickness $h_{c,1} \approx 35-40$ μm below which the orientation of the layers is homeotropic and imposed by the glass. Although the instability is also driven by two different anchorings at the interfaces, the texture is somewhat different from Fig. 2. The glass is indeed far more rigid than the L_α layers, and no depression is observed (see Fig. 5). On the other hand, we have demonstrated the presence of a curvature wall that separates a homeotropic region and the defect itself. The side views of the defects [15] have shown that the shape of the wall is nearly conical, as drawn in Fig. 5.

The lattices of Ref. [15] were obtained by a slow growth process. In order to study their stability, we have checked that they are also formed by the second method, where the

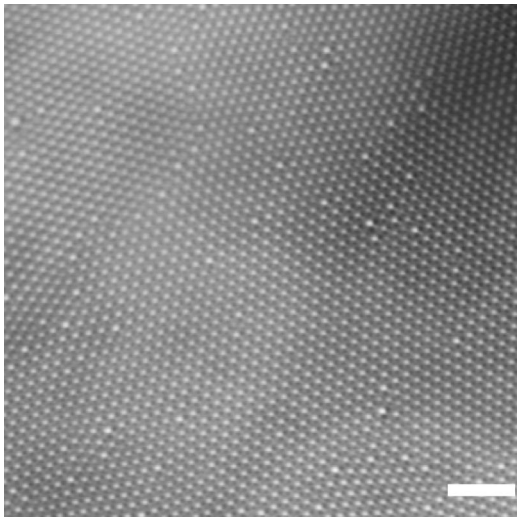

FIG. 6. Hexagonal lattice obtained in a thin slab ($h \approx 65$ μm) of L_α phase. Note that the picture is not perfectly focused in order to make the defects more visible. Each white spot is a single TFCD. Bar 100 μm.

slab is obtained from the contact of the lamellar nuclei with the glass. The observed textures are characterized by the presence of large single-crystals of defects (see Fig. 6) separated by grain boundaries. This shows that the hexagonal lattice is not only obtained by a slow growth process, but formed from the nuclei of lamellar phase in contact with the glass. It should be noted that defects in the grain boundaries are often more visible than other defects. The size of a defect indeed depends on the local organization. Figure 7 shows that the size of a defect depends strongly of the number of its neighbors. We have circled the two largest and smallest defects present in the micrograph. The respective numbers of their neighbors are 7 and 5, i.e., the observed defect is itself a defect (disclination) of the hexagonal array. In the following we shall use ''defect'' to describe elements of the tiling, whether the considered defect belongs to a perfect array or not. We have also circled an empty interstice which is not

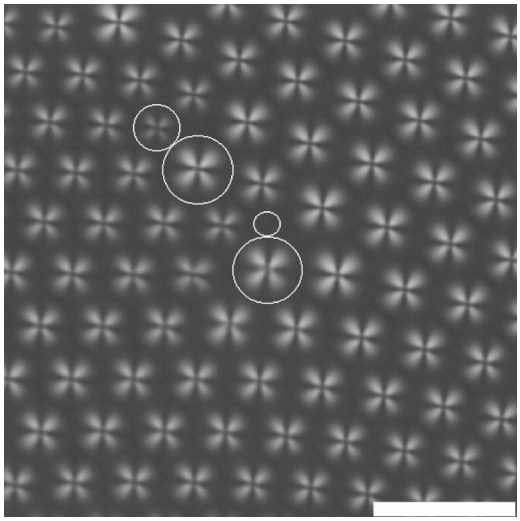

FIG. 7. In a grain boundary, the local hexagonal arrangement of the defects is not present everywhere. The size of the defects depends strongly of the local organization. Bar 50 μm.

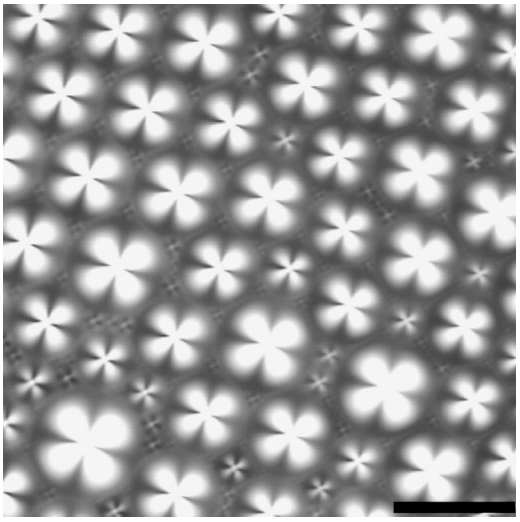

FIG. 8. A typical texture observed above $h_{c,2}$ exhibits a large distribution of sizes (plotted in Fig. 9). Note, however, that a hexagonal lattice can be observed locally (top left). Bar 100 μm. Thickness $h \approx 900$ μm.

filled by a defect. For each thickness there exists a minimal radius below which an empty interstice is not filled, that is the minimal size of the defects here is much larger than the size of the interstices of the HL. Note eventually that this behavior is strongly reminiscent of defects present in the lattices of magnetic bubbles observed in thin magnetic materials submitted to a magnetic field [16].

2. Thicker slabs

The regular lattice HL is no longer observed above another critical thickness $h_{c,2} \approx 200-300$ μm. Even after a few days at rest, the texture does not feature a perfect hexagonal lattice, but rather exhibits a broad distribution of the size of the defects as shown in Fig. 8. We give a histogram of this micrograph in Fig. 9, which nevertheless shows that two different sizes are present in the texture. The first is the characteristic size of the largest defects which are the most visible in Fig. 8. The second is the size of the smallest defects which fill the interstices between the largest ones. The two

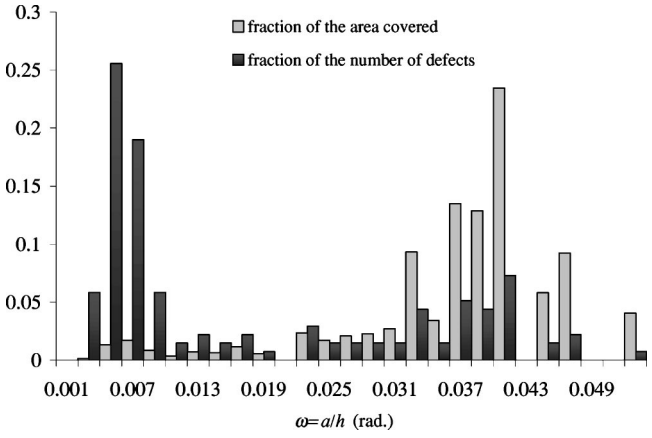

FIG. 9. Histogram of the defects observed in Fig. 8, where ω is the ratio between the radius a of a defect, and $h = 900$ μm is the thickness of the sample. We have represented the distribution of sizes and the distribution of the area covered by the defects.

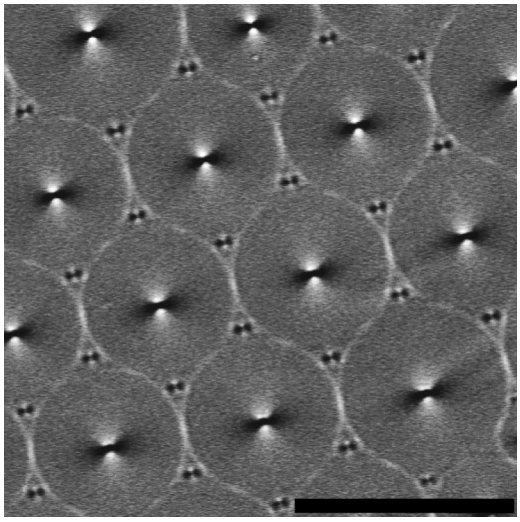

FIG. 10. Local hexagonal lattice with two different sizes of defects. The smaller ones fill the interstices between the larger ones. We have subtracted a part of the background to the micrograph in order to make the contacts between defects more visible. Thickness 780 μm. Bar 100 μm.

types of defects are perfectly visible in the local hexagonal lattices HL_1 which are observed locally (for example in the top left corner of Fig. 8). The two different sizes shown in Fig. 10 are then well defined, since the packing of the larger defects gives the sizes of the second generation of defects in close contact.

The study of the local hexagonal arrangement gives a third critical thickness $h_{c,3} \approx 800-1000$ μm, above which three different sizes of defects are present in the local lattice HL_2 (see Figs. 11 and 12) which replaces HL_1. The thickness $h_{c,3}$ is poorly defined because the appearance of a third generation of defects does not occur at the same time. We show this phenomenon in Fig. 13, where we mark the defects of the third generation appearing in a local HL_1.

In conclusion, the hexagonal lattice seems to be an equilibrium texture, but only for small thicknesses above $h_{c,1}$.

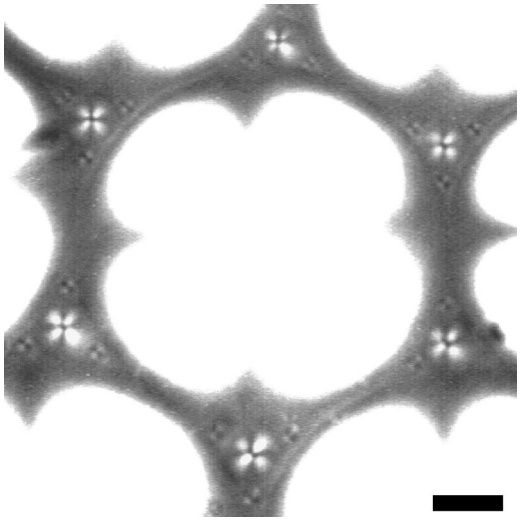

FIG. 11. Above the thickness $h_{c,3}$, the local hexagonal arrangement is made of three types of defects which are the first steps of the Apollonius tiling. In Fig. 12 we give a magnification of the arrangement of the interstices.

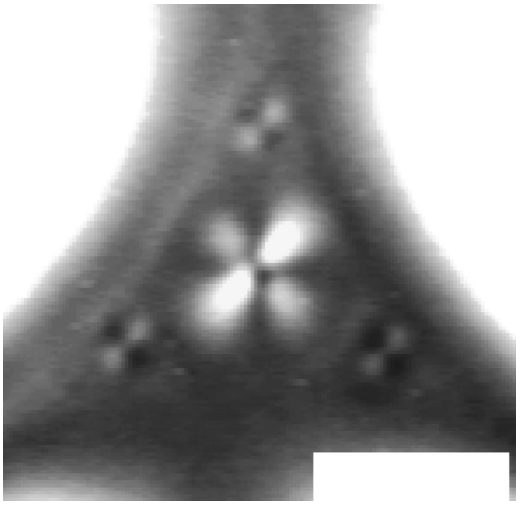

FIG. 12. Local arrangement of the two smallest types of defects in the lattice HL_2 of Fig. 11. Bar 20 μm.

Moreover, we have noted that the size of the defects is not unique but depends on the local organization in the grain boundaries. A second critical thickness $h_{c,2}$ is observed when the HL disappears, and is replaced by a more disordered texture. A regular lattice HL_1 with two sizes of defects is nevertheless observed locally, and is replaced at a third thickness $h_{c,3}$ by the lattice HL_2 in which three different types of defects form the first stages of the Apollonius tiling.

III. THEORETICAL APPROACH

A. Different types of defects

Consider the defects represented in Figs. 2 and 5. They appear in the smectic slab in order to permit a planar anchoring (or a strongly oblique one at an angle θ_0 close to $\pi/2$) at the lower interface, whereas the anchoring remains homeotropic at the upper interface. It is obvious that the classic

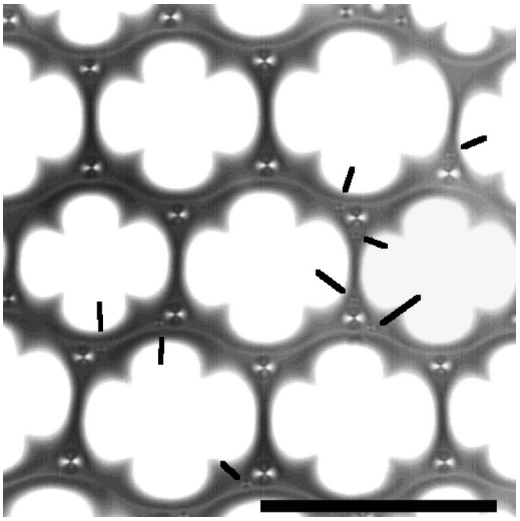

FIG. 13. The appearance of a new generation of defects occurs for a large range of thicknesses. For example, this micrograph represents a local HL_1 in which some defects of the third generation have appeared (their position is given by the black marks). Bar 100 μm. Thickness 910 μm.

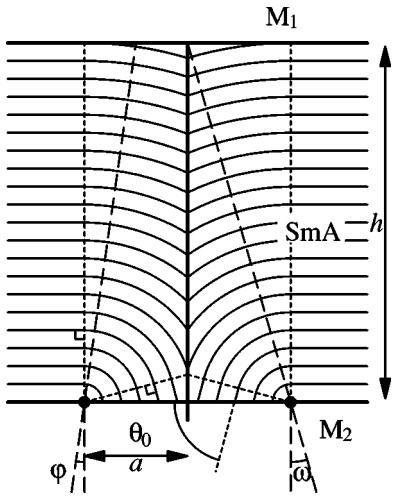

FIG. 14. Model of a TFCD in a Sm*A* phase confined between two flat interfaces with a weak anchoring at the M_1-Sm*A* interface.

''geometric approximation'' (in which the smectic layering remains parallel) is not compatible with a flat upper interface. In the model proposed by Fournier *et al.* [6], each defect carries a small depression at the air-Sm*A* interface, and therefore a slight increase of energy of this interface. In the lyotropic defects, there is no depression but a curvature wall is present, which confines some dilation in the wall. If the homeotropic anchoring were much weaker, another simple model should be considered where the anchoring slightly departs from homeotropy at the upper interface and avoids the dilation in the smectic sample (see Fig. 14). Since the aspect ratio a/h is usually small ($\omega < 0.2$ rad in the experiments reported in Sec. II), we will now use $a = \tan\omega h \approx \omega h$, where ω is the angle defined in the three figures. In all cases, the total free energy of one defect appearing in a planar slab splits into three parts (see Ref. [15] for a discussion of the approximations used).

(i) An energy gain at the lower interface $E_I = -\Delta\sigma\pi a^2$ due to the change of orientation of the layers, where $\Delta\sigma > 0$ is the difference between the interface energy of the homeotropic orientation and the interface energy at the angle θ_0.

(ii) An energy penalty E_c due to the curvature of the layers within the defect. Since ω is so small, this contribution is of the order of the energy of a semi-infinite TFCD, and its main term is $E_c = \alpha\pi K a$, where K is the smectic bending modulus of the layers and α a numerical factor of order 20–30.

(iii) A saturation [17] term E_s due to the presence of the depression, the curvature wall or the departure from the homeotropic anchoring. In the first case, the increase of interface energy of the upper interface is

$$E_s = \Sigma \int_{\varphi=0}^{\omega} 2\pi(a - h\sin\varphi) h \mathrm{d}\varphi - \Sigma\pi a^2 \approx \frac{\pi h^2 \Sigma \omega^4}{12}, \tag{1}$$

where Σ is the free interface energy of the upper interface. For the lyotropic system of Sec. II, the energy penalty is due to the curvature wall of energy per unit area $2K\omega^3/3\lambda$, where λ is the smectic penetration length [15]. The saturation term is therefore

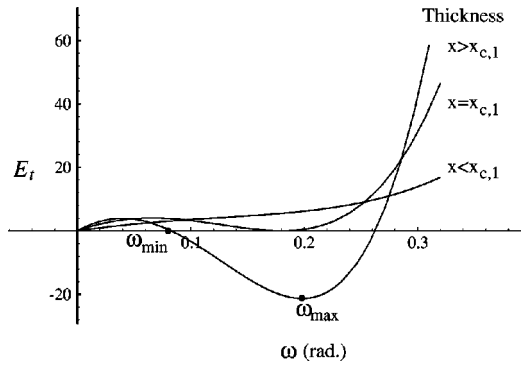

FIG. 15. Variation of the energy of an isolated defect with the geometrical parameter ω for different thicknesses x ($x=50$, 128, and 200). A defect is stable only above the thickness $h_{c,1}=x_{c,1}\alpha\lambda$.

$$E_s=\frac{2\pi K\omega^4 h^2}{3\lambda}. \tag{2}$$

For the case of a weaker anchoring, the increase of area of the upper interface or the dilation of the layers are avoided by a departure of the homeotropic anchoring. Let $W(\varphi)$ be the energy by unit area of the upper interface when the layers are tilted at a small angle φ (see Fig. 14). The expansion of $W(\varphi)$ about its minimum $\varphi=0$ yields $W(\varphi)\approx W_0+(\partial^2 W/\partial\varphi^2)|_0(\varphi^2/2)$, and E_s is given by

$$E_s=\int_{\varphi=0}^{\omega} 2\pi h(\tan\omega-\tan\varphi)W(\varphi)d(h\tan\varphi)-W_0\pi a^2$$

$$\approx\frac{\pi h^2\omega^4\left.\frac{\partial^2 W}{\partial\varphi^2}\right|_0}{12}. \tag{3}$$

The resulting energy of an *isolated defect* in units of $\alpha^2\pi K\lambda$ can therefore be written as

$$E_t(x,\omega)=-\Phi x^2\omega^2+x\omega+\Phi_1 x^2\omega^4, \tag{4}$$

where $\Phi=\Delta\sigma\lambda/K$, $x=h/\alpha\lambda$ is the dimensionless thickness of the slab and $\Phi_1=\Sigma\lambda/12K$, 2/3, or $(\partial^2 W/\partial\varphi^2)\lambda/12K$ according to the relevant model. In the following graphs, we will use the values obtained from Ref. [15]: $\Phi=0.065$, $\Phi_1=2/3$, and $\alpha\lambda=0.3$ μm. The variation of the energy E_t of an isolated defect with the thickness and the angle ω is shown in Fig. 15. There exists a critical thickness $x_{c,1}$ ($x_{c,1}\approx 128$ for the L_α slab considered here), below which a defect has a positive energy and is unstable, whereas a range of possible sizes corresponding to negative values of the energy occurs in thicker samples.

Note eventually that the final expression given in Eq. (4) is not a Taylor expansion of the free energy according to ω, since we have retained only the leading term of each source of energy. However, since we consider cases in which these terms compete, each remaining term is much smaller than the leading term of Eq. (4), and the energy is well approximated by this polynomial expression, as detailed in the Appendix.

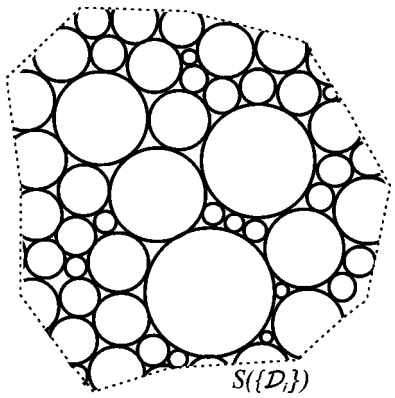

FIG. 16. Since two defects do not intersect in the bulk, the smectic texture of the slabs is represented by a packing of disks of different sizes in the plane.

B. Properties of the packings of defects

We showed in Ref. [15] that the variation with thickness of the size of the defects in the hexagonal lattice is compatible with such an expression of the energy, but we did not consider different arrangements of the defects. We now assume that the experimental observations reported in Sec. II reflect the minimization of the total free energy of the packings of defects. We establish some properties of the packings in the frame of such a hypothesis.

Consider an assembly $\mathcal{D}_i$ of defects represented by their singular circle at the lower interface (see Fig. 16). The total energy of the texture defines an interface energy Σ_e,

$$\Sigma_e(\{\mathcal{D}_i\})=\frac{\sum_{\mathcal{D}_i} E_t(x,\omega_i)}{\mathcal{S}(\{\mathcal{D}_i\})}, \tag{5}$$

when the total area $\mathcal{S}(\{\mathcal{D}_i\})$ of the texture is much larger than the size of one defect. Note that this area is not only the total area of the disks but also includes the interstices. Now consider a single defect of this texture. If it has a radius lower than $x\omega_{min}$ (see Fig. 15), its energy is positive. Its disappearance therefore decreases Σ_e. On the other hand, if its radius is larger than $x\omega_{max}$ where ω_{max} is the minimum of $E_t(x,\omega)$, a texture of smaller energy is obtained when decreasing its size to $x\omega_{max}$ without disturbing the surrounding disks.

The size of a defect in a texture is therefore in the range $\Delta=[\omega_{min},\omega_{max}]$ which is shown in Fig. 17. The boundaries

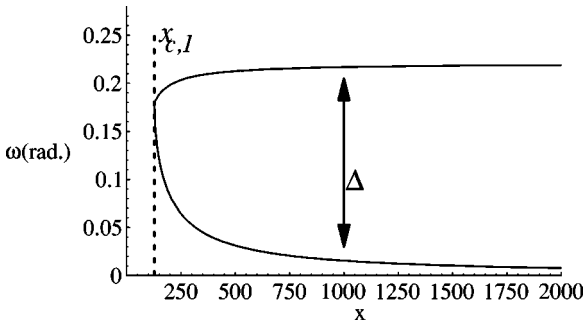

FIG. 17. Range Δ of the possible sizes of the defects as a function of the thickness x.

of Δ are given by

$$E_t(x,\omega_{min})=0, \tag{6}$$

$$\omega_{min}(x)=-2\sqrt{\frac{\Phi}{3\Phi_1}} \times\cos\left(\frac{2\pi}{3}+\frac{\arctan\left(-\sqrt{\frac{4\Phi^3x^2}{27\Phi_1}-1}\right)}{3}\right),$$

$$\omega_{min}(x\to\infty)\approx\frac{1}{\Phi x} \tag{7}$$

and

$$E_t'(x,\omega_{max})=0, \tag{8}$$

$$\omega_{max}(x)=\sqrt{\frac{2\Phi}{3\Phi_1}}\cos\left(\frac{\pi}{3}+\frac{\arctan\left(-\sqrt{\frac{8\Phi^3x^2}{27\Phi_1}-1}\right)}{3}\right),$$

$$\omega_{max}(x\to\infty)\approx\sqrt{\frac{2\Phi}{3\Phi_1}}\cos\frac{\pi}{6}. \tag{9}$$

It should be noted that the range of acceptable sizes increases rapidly above $x_{c,1}$, in contrast to the fact that the regular hexagonal lattices are observed at least up to $h\approx 200$ μm (that is, $x\approx 700$).

It will be useful to define the energy per unit area of one defect by

$$\sigma_e(x,\omega)=\frac{E_t(x,\omega)}{\pi x^2\omega^2}=-\frac{\Phi}{\pi}+\frac{1}{\pi x\omega}+\frac{\Phi_1\omega^2}{\pi}. \tag{10}$$

The interface energy Σ_e of a given texture can therefore be expressed as

$$\Sigma_e(\{\mathcal{D}_i\})=\frac{\sum_{\mathcal{D}_i}\pi x^2\omega_i^2\sigma_e(x,\omega_i)}{\mathcal{S}(\mathcal{D}_i)}. \tag{11}$$

Now, consider a given arrangement $\{\mathcal{D}_i\}$ of the disks. It is stable if the homogeneous dilation of the disks by a factor γ increases the energy,

$$\Sigma_e(\gamma)=\frac{\sum_{\mathcal{D}_i}\pi x^2\gamma^2\omega_i^2\sigma_e(x,\gamma\omega_i)}{\gamma^2\mathcal{S}(\mathcal{D}_i)}, \tag{12}$$

which implies that a stable packing verifies

$$\sum_{\mathcal{D}_i}\omega_i^3\frac{\partial\sigma_e(x,\omega_i)}{\partial\omega}=0. \tag{13}$$

This equation will give us the size of the defects in the texture of minimal energy for a given arrangement. It makes sense to compute this sum on an unit cell when the texture is a regular lattice.

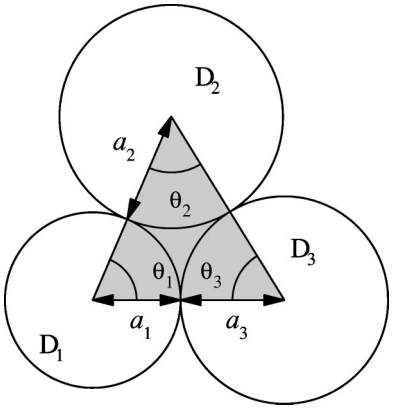

FIG. 18. The vertices of three disks in contact defines the shaded triangle $\mathcal{T}$.

C. Texture of the thin slabs

As shown above, Δ is reduced to a single value only for the thickness $x_{c,1}$. The HL is in this case the most compact arrangement of the disks, and therefore minimizes Σ_e. This geometrical argument can be extended for thicker samples. A lower boundary of Σ_e is indeed given by

$$\Sigma_e\geqslant d(\{\mathcal{D}_i\})\min_{\omega\in\Delta}\sigma_e(\omega), \tag{14}$$

where $d(\{\mathcal{D}_i\})$ is the area fraction occupied by the disks. The exact largest value taken by $d(\{\mathcal{D}_i\})$ for noncongruent disks is known when the ratio of smallest over largest admissible radii is not too small [18]. For $\omega_{min}/\omega_{max}\in[0.743\ldots,1]$, the densest packing is indeed a hexagonal lattice of disks of same size for which $d(\{\mathcal{D}_i\})=\pi/\sqrt{12}\approx 0.907$. Therefore, Eq. (14) becomes an equality for an hexagonal packing of disks with radius $x\omega_0$ where $\sigma_e'(\omega_0)=0$, that is

$$\omega_0(x)=\sqrt[3]{\frac{1}{2\Phi_1 x}}. \tag{15}$$

In Ref. [15], we considered only the existence of hexagonal lattices, and obtained this law, which was in rather good agreement with the experimental data.

Finally, also note that this approach also explains why the size of the defects in a grain boundary deviate from the optimal size of a defect in a HL. This size is indeed not only fixed by the thickness of the slab, but also depends on the local arrangement of the defects.

D. Transitions of texture in the thicker slabs

In order to look if another packing has a lower energy as the thickness increases, we have considered three disks in contact, as shown in Fig. 18. Note the respective radius of the disks, $(a_1,a_2,a_3)=(x\omega_1,x\omega_2,x\omega_3)$, and define an interface energy for the triangle $\mathcal{T}$ (whose vertices are the centers of the disks) by

$$\sigma_t(x,\omega_1,\omega_2,\omega_3)=\frac{\sum_{i=\{1,2,3\}}\theta_i x^2\omega_i^2\sigma_e(x,\omega_i)}{2\mathcal{S}_t(x,\omega_1,\omega_2,\omega_3)}, \tag{16}$$

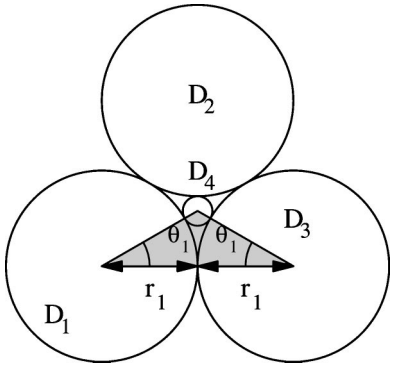

FIG. 19. In the lattice HL_1, the radius r_4 of the small circles is given by $r_4=\beta_1 r_1$.

where θ_i is defined in Fig. 18, and $\mathcal{S}_t$ is the area of the triangle. From geometric considerations, we obtain the following relations (with all the permutations $\{1,2,3\}$):

$$\mathcal{S}_t(x,\omega_1,\omega_2,\omega_3)=x^2\sqrt{\omega_1\omega_2\omega_3(\omega_1+\omega_2+\omega_3)}, \quad (17)$$

$$\cos\theta_1=1-\frac{2\omega_2\omega_3}{(\omega_1+\omega_3)(\omega_1+\omega_2)}, \quad (18)$$

$$\sin\theta_1=\frac{2\sqrt{\omega_1\omega_2\omega_3(\omega_1+\omega_2+\omega_3)}}{(\omega_1+\omega_2)(\omega_1+\omega_3)}. \quad (19)$$

Any triangle $\mathcal{T}(\omega_1,\omega_2,\omega_3)$ tiles the plane, but this does not insure that the disk angles that it carries adjust correctly to perfect full disks in the tiling, except for some special triangles and tilings as in Fig. 19. However, any tiling with a single triangle of lowest σ_t which readjusts the disk angles gives an optimal packing of lowest interface energy $\Sigma_e=\sigma_t$.

We have numerically determined the absolute minimum of σ_t for $(\omega_1,\omega_2,\omega_3)\in\Delta^3$, and we give the resulting triangle as a function of the thickness x in Fig. 20. This latter is equilateral ($\theta_i=\pi/3$) for $x<1040$, and isosceles above this value (we give the values taken by the larger angle θ_2 as a function of x). It therefore shows that the lattice HL is the optimal packing at least up to $x=1040$. Note that this method does not rigorously prove that the HL is no longer the optimal packing above this value, but it can be shown that other textures have a lower energy in the neighborhood

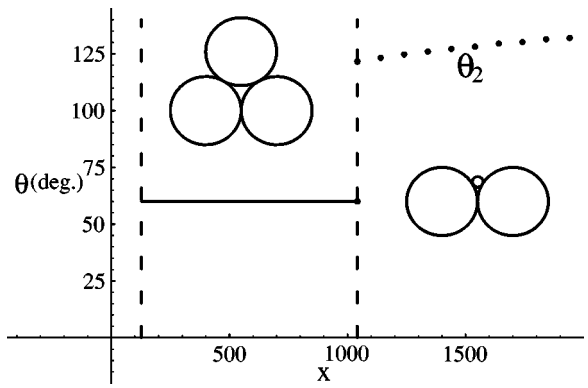

FIG. 20. Assembly of three disks in contact defining the triangle $\mathcal{T}$ of minimal interface energy σ_t according to the thickness x.

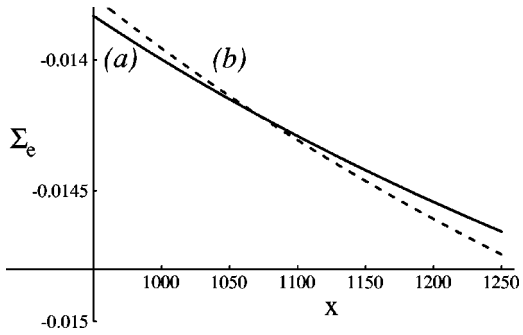

FIG. 21. Evolution of $\Sigma_e(\mathrm{HL})$ (a) and $\Sigma_e(\mathrm{HL}_1)$ (b) . The two curves intersect at $x_{c,1}\approx 1071$.

of this value. For example, let us compare the free energies of the lattices HL and HL_1. Figure 19 shows that the radius $r_4=x\omega_4$ of the smallest disk in a cell of HL_1 is related geometrically to the radius $r_1=x\omega_1$ of the large disks by the Apollonius number $\beta_1\approx 0.1547\ldots$:

$$\omega_4=\left(\frac{2}{\sqrt{3}}-1\right)\omega_1=\beta_1\omega_1. \quad (20)$$

Then applying Eq. (13) in an unit cell, the tiling HL_1 of lowest energy is obtained when

$$\omega_1=\left(\frac{1+2\beta_1}{2\Phi_1 x(1+2\beta_1^4)}\right)^{1/3}. \quad (21)$$

In Fig. 21 we reported the variation of Σ_e for the two lattices, which shows that HL_1 is favored beyond $x_{c,2}=1071$ ($h_{c,2}\approx 290-340$ μm). Note that this last result is rather consistent with the experimental data (see Sec. II).

In HL_2, represented in Fig. 22, the radius of the next generation is $x\beta_2\omega_1$, where

$$\beta_2=\frac{3-4/\sqrt{3}}{11}. \quad (22)$$

The radius of the larger disks $x\omega_1$ is given by Eq. (13):

$$\omega_1=\left(\frac{1+2\beta_1+6\beta_2}{2\Phi_1 x(1+2\beta_1^4+6\beta_2^4)}\right)^{1/3}. \quad (23)$$

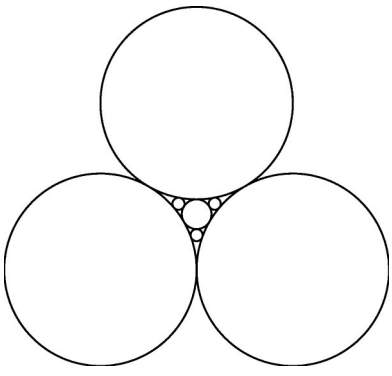

FIG. 22. Local arrangement of the lattice HL_2.

The comparison between $\Sigma_e(HL_1)$ and $\Sigma_e(HL_2)$ then provides a third critical thickness $x_{c,3} \approx 3629$ ($h_{c,3} \approx 1000-1150$ μm) which also agrees with the observed experimental thickness ($h_{c,3} \approx 800-1000$ μm) for which the third generation of defects appears locally, although somewhat larger.

IV. DISCUSSION

We have shown by the above approach that the form of the energy of a *single defect* explains the qualitative features of the *textures* present in thick slabs of L_α phase. The values $\Phi \approx 0.065$ and $\alpha\lambda \approx 0.3$ μm used in Sec. III were obtained in Ref. [15] from the measurement of the first critical thickness $h_{c,1} \approx 35-40$ μm and the geometrical parameters of the corresponding defects. The use of the same values in Sec. III also provided a second critical thickness $h_{c,2} \approx 300$ μm for which HL becomes unstable and is replaced by a less organized texture. Locally the texture HL_1 is favored up to $h_{c,2} \approx 1000$ μm, and beyond this third critical value HL_1 changes to HL_2 which has a lower energy. The corresponding transitions are experimentally observed, which indicates that the actual form of the energy is close to the expression given in Eq. (4).

Concerning the dynamic of formation of the textures, several points require further study. First, we have not explained *how* defects form from the homeotropic slab. In the case the Sm*A* slabs studied by Fournier *et al.* [8], the appearance of a single defect is preceded by a Sm*A*-isotropic interface instability similar to the Mullins-Sekerka mechanism [19], that helps its nucleation. In a lateral geometry [15] and with a slow growth (≈ 1 μm min^{-1}), we have not observed such a large deformation of the L_3/L_α interface, but nevertheless observed the appearance of the defects, which suggests that the energy barrier is lower in this case. However, if we assume that earlier stages of the nucleation are still described by Fig. 5, with ω increasing continuously toward its equilibrium value, the corresponding barrier energy E_b (estimated from Fig. 15) is rather large compared to kT (the unit of E_t is indeed $\alpha^2 \pi K \lambda \approx 10^3 kT$ with the usual orders $K \approx kT/d$ and $\lambda \approx d$, where d is the thickness of the smectic layers). We think that two phenomena actually strongly decrease E_b, which is mainly due to the curvature of the layers [the term $x\omega$ in Eq. (4)]. First, if the orientation of the layers increases continuously from 0 to its equilibrium value θ_0 at the L_3-L_α interface, the large bending energy of the layers associated with the focal conics domains in the nucleating defect can be avoided (see Fig. 23). Second, any irregularity at the glass substrate tends to deform the layers, and therefore strongly decreases the barrier. Such irregularities could be very efficient seeds for the defects which move easily once formed.

A second interesting point is the dynamical formation of the hexagonal lattices. Indeed we think that the spontaneous organization of defects in the thin slabs is due to the existence of a finite range of sizes for the defects, and that the situation here is very different from the organizations of single-sized disks in the plane which would form random close packings. The continuous variation of size could help to overcome some geometric lockings during the formation of the lattices. Such rearrangements should, however, be limited to small thicknesses, which correspond to not too large

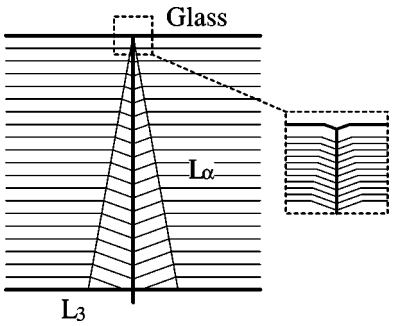

FIG. 23. Two main mechanisms are expected to lower the energy barrier of the nucleation of one defect: the penalty due to the curvature energy can be reduced, first, by an anchoring at angles smaller than θ_0 at the L_3/L_α interface, and second by the presence of irregularities at the glass substrate which favors the tilt of the layers and the nucleation of the defects.

values for the range of variation Δ of the defect size. For larger thickness, the formation of local lattices HL_1 and HL_2 is not expected to come from a global rearrangement of the defects, but rather from the nucleation of defects inside the interstices. The typical size of the largest defects remains close to ω_0, because this value corresponds to the minimal interface energy Σ_e at the scale of the disk. The characteristic size of the interstices between three large disks in contact is therefore given by $\beta_1 \omega_0$, and enters the range Δ when the thickness increases, which permits the appearance of a defect inside the interstice. The same mechanism is also expected for other generations which appear in smaller empty interstices at larger thicknesses.

V. CONCLUSION

In this work, we discussed the arrangement of defects present in a slab of smectic phase in contact with two parallel interfaces and different boundary conditions. The toric focal conics domains occurring above a first critical thickness form a regular hexagonal lattice in thin slabs. The size of the defects is fixed not only by the thickness but also depends on the local order, i.e., the deviations from hexagonal order, and is therefore different in grain boundaries. When the thickness increases, the regular lattices are unstable and become disor-

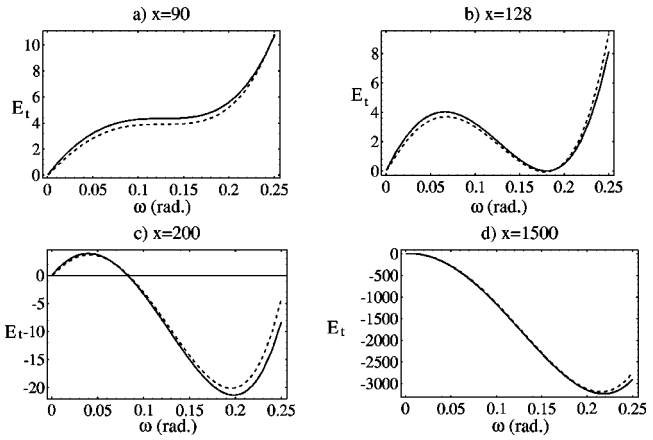

FIG. 24. Comparison of the energy of a single defect given by Eq. (4) (plain lines) and Eq. (A1) (dashed lines) for different thicknesses x ($C=0.59$, $\alpha=30$, and $\Phi=0.065$).

dered on a large scale. We have shown that regular assemblies are nevertheless locally observed. In these textures, defects form the first stages of Apollonius packings of disks in a plane. We have modeled a defect by a disk in the plane, and computed its surface energy. The minimization of the total surface energy of assemblies of noncongruent disks reproduces the main features of the textures, and explains the presence of different transition thicknesses.

We have also shown that the main type of saturating term for the energy of a single defect (deformation of the interface, dilation or energy of anchoring) has the same dependence in the geometrical parameters of the defects. We therefore expect that similar behaviors should be observed in other smectic systems.

APPENDIX

In this appendix, we compare the energy of the defect sketched in Fig. 5 to the polynomial expression given in Eq. (4). The exact free energy (in units of $\alpha^2 \pi K \lambda$) of the defects sketched in Fig. 5 is given by [15]

$$E_t(x,\omega) = -\Phi x^2 \tan^2\omega + 2x^2 \frac{\tan\omega - \omega}{\sin\omega}\tan^2\omega + \frac{2\tan\omega x}{\alpha}\left\{[\ln(\alpha x \tan\omega) - 2](\theta_0 - 2\omega) - \int_{\pi/2-\theta_0}^{\pi/2-2\omega} \ln\cos\varphi \, d\varphi\right\}$$

$$+ \frac{x\tan\omega}{\alpha}[\ln(\alpha x\tan\omega) - 1][\sin^2 2\omega(\tan^{-1}\omega - \tan^{-1}2\omega) + \sin^2\theta_0/\tan\theta_0] + Cx\tan\omega, \quad \text{(A1)}$$

where the first and second terms represent the gain of energy at the L_α-L_3 interface and the energy of the conical wall, whereas the other terms account for the curvature energy of the layers sketched in Fig. 5. C is a constant of order unity which accounts for the energy of the straight line defect [15], and we have taken λ as a value of the cutoff lengths which appear in the neighborhood of the two line defects. Figure 24 shows that the main features of E_t are correctly described by the much simpler expression given in Eq. (4).

[1] G. Friedel, Ann. Phys. (Paris) **18**, 273 (1922).

[2] P.-G. De Gennes and J. Prost, *The Physics of Liquid Crystals* (Clarendon, Oxford, 1993).

[3] P. Boltenhagen, M. Kleman, and O. D. Lavrentovich, in *Soft Order in Physical Systems*, edited by Y. Rabin and R. Bruinsma (Plenum Press, New York, 1994), p. 5.

[4] P. Boltenhagen, M. Kleman, and O. D. Lavrentovich, C. R. Seances Acad. Sci., Ser. B **52**, 931 (1992).

[5] P. Boltenhagen, O. D. Lavrentovich, and M. Kleman, Phys. Rev. A **46**, R1743 (1992).

[6] J.-B. Fournier, I. Dozov, and G. Durand, Phys. Rev. A **41**, 2252 (1990).

[7] J.-B. Fournier, Ph.D. thesis, University Paris Sud, 1991 (unpublished).

[8] J.-B. Fournier, M. Warenghem, and G. Durand, Phys. Rev. E **47**, 1144 (1993).

[9] C. Quilliet, C. Blanc, and M. Kléman, Phys. Rev. Lett. **77**, 522 (1996).

[10] G. Porte, J. Marignan, P. Bassereau, and R. May, J. Phys. (Paris) **49**, 511 (1988).

[11] D. Anderson *et al.*, J. Phys. Chem. **93**, 4243 (1988).

[12] D. Gazeau *et al.*, Europhys. Lett. **9**, 447 (1989).

[13] D. Roux *et al.*, Europhys. Lett. **11**, 229 (1990).

[14] D. Filali *et al.*, J. Phys. II **4**, 349 (1994).

[15] C. Blanc and M. Kleman, Eur. Phys. J. B. **10**, 53 (1999).

[16] A similar micrograph for bubbles in magnetic materials can be found in P. M. Chaikin and T. C. Lubensky, *Principles of Condensed Matter Physics* (Cambridge University Press, Cambridge, 1995), p. 518. The original paper is by M. S. Seul and C. A. Murray, Science **262**, 558 (1993). For a review on bubble domains, also see A. P. Malozemoff and J. C. Slonczewski, *Magnetic Domain Walls in Bubble Materials* (Academic Press, New York, 1979).

[17] We keep the terminology of Fournier *et al.* [6]. This term prevents an isolated defect of too great an increase in its size.

[18] A classic text on the tiling of noncongruent disks can be found in L. Fejes Tóth, *Regular Figures* (Pergamon Press, Oxford, 1964).

[19] W. W. Mullins and R. F. Sekerka, J. Appl. Phys. **35**, 444 (1964).